

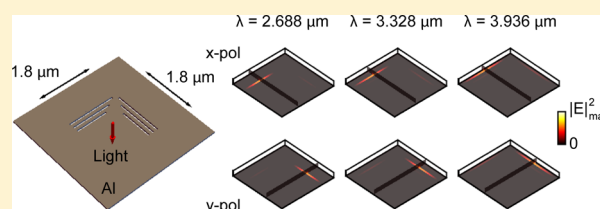
Planar, Ultrathin, Subwavelength Spectral Light Separator for Efficient, Wide-Angle Spectral Imaging

Yasin Buyukalp,^{*†} Peter B. Catrysse,^{*†} Wonseok Shin,[†] and Shanhui Fan^{*}

E. L. Ginzton Laboratory and Department of Electrical Engineering, Stanford University, Stanford, California 94305, United States

ABSTRACT: We propose a planar, ultrathin, subwavelength spectral light separator that enables efficient, angularly robust, spatially coregistered decomposition of light into its spectral components. The device consists of a collection of spectrally tuned “meta-atoms” and achieves spectral selectivity by utilizing strong localized resonance supported by each individual meta-atom. The three-dimensional meta-atoms are formed by resonant subwavelength-size rectangular apertures in a planar metallic film of deep-subwavelength thickness. The overall physical cross-sectional area of the device is subwavelength, and its thickness is deep-subwavelength. Different spectral components of light are simultaneously separated and collected in different subwavelength-size aperture pairs, where each aperture pair is composed of two perpendicularly oriented, same-size apertures; and different aperture pairs collect their light from overlapping cross-sectional regions. Hence, spatial coregistration errors between different spectral channels are quite reduced, which is an attractive feature for multispectral imaging systems. The operation of the device is polarization-independent; however, the device also simultaneously separates different linear polarization components of light and collects their power in different apertures of aperture pairs. The device also exhibits angular robustness for obliquely incident light, that is, spectral selectivity is largely angle-independent. Both features are appealing for imaging applications.

KEYWORDS: multispectral imaging, snapshot systems, polarimetric imaging, subwavelength, Fabry-Pérot, nanocavities, apertures, metallic structure, funneling



In many areas of science and technology that utilize the spectrum of light, such as spectroscopy, multispectral imaging, hyperspectral imaging, and wavelength demultiplexing, it is desired to decompose light into its spectral components with minimum photon loss.^{1–20} Especially, in snapshot imaging applications, where the goal is to simultaneously collect full spatial and spectral information, one needs to perform the spectral decomposition in a photon-efficient manner, without sacrificing spatial resolution, which is conventionally limited by diffraction.^{5,21,22} Furthermore, imaging systems are increasingly miniaturized, and pixels in image sensors or focal plane arrays tend to shrink down to the (sub)wavelength scale, which are driven in part by the small form factor requirement on mobile platforms.^{8,22–27} Hence, there is an urgent need for a photon-efficient, compact, subwavelength-size spectral light separator to build high-resolution, low-cost, low-power, and lightweight multispectral snapshot imaging systems.^{1–8,21,26}

One class of snapshot systems achieves spectral selectivity by utilizing hard-to-miniaturize devices that are larger than their operating wavelength in size.^{5,11,17–19,28–40} Traditionally, these systems include either spectral decomposition systems based on prisms or guided-mode resonance filters based on phase-matching elements such as diffraction gratings.^{5,8,11,28,29} Novel devices have also been proposed, such as photon sorters or other plasmonic structures.^{17–19,30–40} Their operation depends on surface plasmon polariton excitation by using periodic hole arrays, groove arrays, or gratings, where the period is comparable to the operation wavelength. To operate, these

devices require at least a few periods; therefore, they are necessarily larger than the operation wavelength.⁴¹

As an alternative approach, spectral selectivity can be achieved with structures supporting localized resonances.^{7,13,42,43} Recently, the concept of assembling several deep-subwavelength resonant structures (“meta-atoms”), each supporting a single resonance at a different wavelength, to achieve spectral separation at the subwavelength scale in a single isolated (i.e., nonperiodic) device was demonstrated.^{7,13} This concept does not rely on any periodicity effect to achieve spectral separation. It is therefore compatible with the current trend in constructing detector arrays with smaller, (sub)-wavelength-size pixels. Unlike spectral filter arrays, where only a single spectral component is selected in a wavelength-size pixel area, the devices based on this concept select and separate multiple spectral components in a subwavelength-size area; therefore, this concept also provides a more photon efficient way for imaging than the concept of using spectral filter arrays.

The subwavelength-size devices that have been demonstrated so far,^{7,13} however, remain polarization-dependent, which is not ideal for many imaging applications. Moreover, for spectral separation, they utilize either strong interference between different spectral bands¹³ or nonplanar structures.⁷ The former limits spectral selectivity, angular robustness, and hence

Received: September 16, 2016

Published: January 17, 2017

efficiency. The latter results in thickness that is not deep-subwavelength and poses fabrication challenges.

RESULTS AND DISCUSSION

In this work, we numerically demonstrate a planar subwavelength spectral light separator that overcomes all the above-mentioned limitations associated with previously demonstrated spectral separation devices. We present here a three-dimensional (3D), surface-thin, planar, subwavelength-size nanophotonic device that can decompose light into its spectral components in a very photon-efficient way. Our spectral light separator achieves spectral selectivity by utilizing the strong localized resonances of 3D meta-atoms formed by subwavelength resonant apertures in a metallic film of deep-subwavelength thickness. These apertures have electromagnetic cross sections far exceeding their physical size at their resonance wavelengths.⁴⁴ We show that one can assemble these apertures, each tuned to a different wavelength, in a subwavelength-wide and deep-subwavelength-thick device without causing significant interference among them. The overall transmission through our device is polarization-independent, but the device can be used to separate the different linear polarization components of light as well, which might be useful for polarimetric imaging.^{17,38} We also show that our device has angular robustness, that is, a clear spectral separation can still be achieved for obliquely incident light. Furthermore, since the apertures collect light coming from overlapping cross-sectional regions, spatial coregistration errors between different spectral channels are quite reduced, which is a very attractive feature for multispectral imaging.^{7,45,46}

Figure 1 illustrates a planar subwavelength spectral light separator designed to operate at infrared wavelengths. The

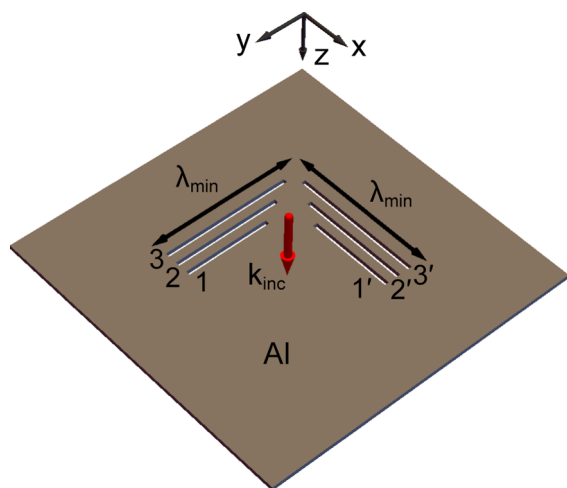


Figure 1. Geometry of the proposed planar subwavelength spectral light separator. The device consists of three rectangular aperture pairs where each aperture pair is composed of two perpendicularly oriented, same-size, air-filled apertures in a deep-subwavelength-thick aluminum film. The structure is isolated (non-periodic). The film thickness is 50 nm. Each aperture has a width and height of 50 nm. Each of the apertures of the first aperture pair (1–1′) has the length of 1 μm , of the second aperture pair (2–2′) has the length of 1.25 μm , and of the third aperture pair (3–3′) has the length of 1.5 μm . The separation between adjacent parallel apertures is 200 nm. The device is surrounded by air. k_{inc} represents the incident light. λ_{min} is 1.8 μm , which corresponds to the minimum free-space wavelength size in the investigated spectral range.

structure is a single isolated (i.e., nonperiodic) device. It consists of three subwavelength-size rectangular aperture pairs (1–1′, 2–2′, and 3–3′) in an ultrathin metallic film. The film thickness is 50 nm, which is deep-subwavelength compared to the operating wavelength range. The apertures have a width of 50 nm, and their lengths are chosen such that each aperture exhibits a resonant behavior at a single spectral band in the wavelength range between 1.8 and 5 μm . Each of the apertures of the first aperture pair (1–1′) has the length of 1 μm , of the second aperture pair (2–2′) has the length of 1.25 μm , and of the third aperture pair (3–3′) has the length of 1.5 μm , which allows separating three different spectral components of light such that each spectral component is transmitted through a different aperture pair. For each aperture pair, one aperture is oriented along the x -direction, and the other aperture is oriented along the y -direction, which enables a polarization-independent response when using aperture pairs as detected elements. The separation between adjacent parallel apertures is 200 nm. The overall structure is symmetric with respect to the $x = y$ plane. The total physical cross-sectional area of the device is in the subwavelength range. Without loss of generality, we choose aluminum⁴⁷ (Al) as the metal, choose air as the material surrounding the device, and use air-filled apertures. We also examine the case where the metal is perfect electric conductor (PEC) to compare its performance with that of the realistic Al device and to provide a simpler understanding of the operation principle. We demonstrate the operation of our device by simulating its interaction with electromagnetic waves via the finite-difference frequency-domain (FDFD) method.^{48–50}

Figure 2 shows the transmission cross section spectra, $\sigma_T(\lambda)$, calculated when the incident light is a normally incident plane wave with its electric field along the x -direction (x -polarized). The individual transmission cross section spectra of the aluminum structure in Figure 2a–c show clear resonance behavior at three different infrared wavelengths, which are 2688, 3328, and 3936 nm. As can be seen in the figure, these resonances are associated with the first (aperture 1), second (aperture 2), and third (aperture 3) aperture oriented along the y -direction, respectively. Thus, different resonances occur in the different apertures, meaning that the spectral separation is achieved. Note that these resonances correspond to the three resonance peaks in the overall transmission cross section spectra shown in Figure 2d. We observe that the peak wavelengths of the transmission cross section resonances depend directly on the lengths of the apertures oriented along the y -direction. Also, the ratios of the resonance wavelengths are approximately equal to the ratios of the lengths of the corresponding resonant apertures. This is because the resonances are associated with Fabry-Pérot-like cavity modes that are supported by the subwavelength rectangular apertures for incident light having an electric field component pointing along the apertures' short axis.^{51,52} This behavior can be clearly noticed by investigating the transmission cross section spectra of the PEC structure, where each resonance wavelength is approximately twice the length of the corresponding resonant aperture, with a small redshift due to the electromagnetic coupling to free-space modes.^{51,53} In the case where the metal is aluminum, there is an additional redshift in each resonance wavelength. This is attributed both to the penetration of the electromagnetic fields into the aluminum film due to the finite dielectric constant of the aluminum, and to the coupled surface waves that are supported

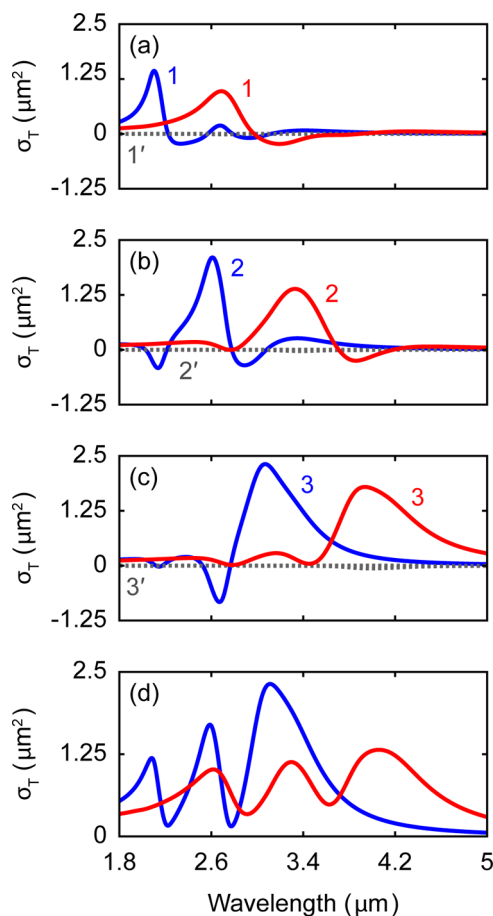


Figure 2. Transmission cross section spectra of both aluminum and PEC planar subwavelength spectral light separators for a normally incident x -polarized plane wave. The individual transmission cross section spectra for the aperture pair 1–1' in a), 2–2' in b), and 3–3' in c). The blue line corresponds to the individual transmission cross section spectrum of the Aperture 1 in a), 2 in b), and 3 in c) for the PEC structure whereas the red line corresponds to the individual transmission cross section spectrum of the Aperture 1 in a), 2 in b), and 3 in c) for the aluminum structure. In each of a), b) and c), there are two separate dotted-gray lines coinciding almost on top of each other, and they show the individual transmission cross section spectra of the Aperture 1' in a), 2' in b), and 3' in c) for the PEC structure and the aluminum structure. (d) The overall transmission cross section spectra for the entire structure. The blue line corresponds to the PEC structure whereas the red line corresponds to the aluminum structure.

at the aluminum-air interfaces on the long edges of the resonant apertures.^{52,54}

The peak transmission cross section of each resonant aperture is much larger than the physical size of the aperture. The peak transmission cross sections of the aluminum structure are 0.971, 1.3873, and 1.7944 μm^2 for the first, second, and third resonant aperture, respectively. The physical sizes of these apertures are 0.05, 0.0625, and 0.075 μm^2 respectively. Thus, the peak transmission cross sections are more than 19 times the physical area of the apertures. For the PEC structure, the peak transmission cross sections are 1.4355, 2.1034, and 2.315 μm^2 for the first, second, and third resonant aperture, respectively. Each of these values is very close to the maximum theoretical transmission cross section of a single deep-subwavelength rectangular aperture in a PEC film, which is approximately $3\lambda^2/4\pi$.^{51,53,55} This limit arises from the fact that a single deep-

subwavelength rectangular aperture has a radiation pattern very close to a dipole radiation pattern. Compared to the PEC structure, the aluminum structure has about 32.4%, 34%, and 22.5% less peak transmission cross section for the first, second, and third resonant aperture, respectively. This reduction is due to the finite and lossy dielectric constant of aluminum. Still, the aluminum structure maintains the resonant behavior. Hence, our device composed of the realistic metal is capable of funneling and collecting light at the selected wavelengths.

Another important figure of merit in imaging applications is the ratios of the individual transmission cross sections to the overall active device area. These ratios also correspond to the individual transmittances. In a periodic device, the overall active device area of each period can be clearly defined as the area of the period. However, the isolated structure simulation we performed here corresponds to a metal film that has an infinite size in x - and y -direction with only six apertures on it, and therefore, the active device region cannot be chosen unambiguously. Hence, for the isolated planar subwavelength spectral light separator shown in Figure 1, we prefer to discuss the transmission cross section spectra, and later in the paper, we discuss the transmittance spectra of the aluminum planar subwavelength spectral light separator array shown in Figure 4.

The individual transmission cross section spectra of the apertures oriented along the x -direction (apertures 1', 2', and 3') show negligible transmission in Figure 2a–c because the operation wavelength range is above the cutoff wavelengths of these apertures for x -polarized incident light. Above the cutoff wavelength, fields inside these apertures are evanescent and the coupling of the apertures with the incident wave is very poor; thus, the transmission through these apertures decreases strongly with an increase in wavelength above the cutoff wavelength.⁵¹

Our structure is symmetric with respect to the $x = y$ plane. Thus, by doing additional simulations, we observed that the individual transmission cross section response of an aperture oriented along the y -direction when illuminated by x -polarized light and the response of the same-size aperture oriented along the x -direction when illuminated by y -polarized light are the same. Also, the overall transmission cross section spectra obtained for x -polarized light and y -polarized light are identical, meaning that the overall transmission properties of the device are independent of the light polarization in the case of normal incidence.

Although the apertures are physically very close to each other compared to their operation wavelengths, different apertures efficiently collect light with different wavelengths and polarizations. To make a quantitative statement, we define the spectral crosstalk between a resonant aperture and an off-resonant aperture as the ratio of the mean absolute transmission cross section of the off-resonant aperture to the mean absolute transmission cross section of the resonant aperture in the spectral band of the resonant aperture. The spectral band of the resonant aperture is defined as the wavelength range corresponding to the full width at half-maximum (fwhm) of the transmission cross section spectrum of the resonant aperture. If we define $\lambda_{1,i}$ and $\lambda_{2,i}$ such that they correspond to the wavelengths at which the transmission cross section of the resonant aperture i has half of its peak value and $\lambda_{2,i} > \lambda_{1,i}$, the difference of those wavelengths ($\lambda_{2,i} - \lambda_{1,i}$) corresponds to the full width at half-maximum (fwhm) of the transmission cross section spectrum of the resonant aperture i . Then, the spectral

Table 1. Spectral Crosstalk (ω_{ij}) between a Resonant Aperture i and an Off-Resonant Aperture j for the Aluminum Subwavelength Spectral Light Separator Excited by a Normally Incident x -Polarized Plane Wave

		off-resonant aperture j					
		1	2	3	1'	2'	3'
resonant aperture i	1		0.1218	0.1306	0.0096	0.0010	0.0002
	2	0.1351		0.1539	0.0014	0.0177	0.0025
	3	0.0231	0.0759		0.0003	0.0028	0.03

crosstalk (ω_{ij}) between the resonant aperture i and the off-resonant aperture j is given by the formula below.

$$\omega_{i,j} = \frac{\frac{1}{\lambda_{2,i} - \lambda_{1,i}} \int_{\lambda_{1,i}}^{\lambda_{2,i}} |\sigma_{T,j}(\lambda)| d\lambda}{\frac{1}{\lambda_{2,i} - \lambda_{1,i}} \int_{\lambda_{1,i}}^{\lambda_{2,i}} |\sigma_{T,i}(\lambda)| d\lambda} = \frac{\int_{\lambda_{1,i}}^{\lambda_{2,i}} |\sigma_{T,j}(\lambda)| d\lambda}{\int_{\lambda_{1,i}}^{\lambda_{2,i}} |\sigma_{T,i}(\lambda)| d\lambda}$$

For the aluminum structure, the spectral band of the aperture 1 is the wavelength range between 2433 and 2844 nm; the spectral band of the aperture 2 is the wavelength range between 3074 and 3558 nm, and the spectral band of the aperture 3 is the wavelength range between 3702 and 4425 nm. The spectral crosstalk values for the aluminum structure are given in Table 1.

Table 1 shows that the spectral crosstalk between the apertures oriented along y -axis and x -axis are almost zero as expected from the fact that the incident light is x -polarized. Also, the maximum spectral crosstalk between any resonant aperture and off-resonant aperture is less than 15.4%. Thus, only the resonant aperture effectively transmits light in its spectral band, and the transmission cross section of each aperture is very small for all of its off-resonance conditions. As a result of these, we can see that the transmission cross section spectra shown in Figure 2 exhibit very small spectral crosstalk.

As a further evidence of the lack of a major spectral crosstalk in this structure, Figure 3 shows the electric field intensity ($|E|^2$) distribution of the aluminum structure at the resonance wavelength and the resonance polarization of each aperture. In each case, the field intensity is predominantly concentrated in only one aperture. Thus, light is funneled into a single aperture at each pair of resonance wavelength and polarization.

As an additional note, the individual transmission cross section spectra in Figure 2a–c show that negative transmission occurs through off-resonant apertures in some parts of the spectral region. Near the resonance wavelength of each aperture, there is negative power flow through the off-resonant apertures. Thus, some transmitted power through the resonating apertures flows back to the input side through the off-resonant apertures. We observed a similar phenomenon in our previous work⁷ on a nonplanar spectral light separator, and we believe that this phenomenon is related to the observations of negative power flow in periodic arrays of compound apertures.⁵⁶ On the other hand, as can be seen in Figure 2d, the values of the overall transmission cross section spectra are all above zero. Hence, these results show that even when there is negative power flow through off-resonant apertures, the total transmitted power flow through the entire structure remains positive, as expected.

In general, by tuning the geometrical properties and the orientation of the apertures, one can control their resonance behavior. For the structure shown in Figure 1, the width, length, and height of each aperture control the aperture's resonance wavelength, while the orientation of each aperture controls its polarimetric response. We have observed that an increase in the length of a resonating aperture causes a major

redshift in the resonance wavelength of the aperture due to Fabry-Pérot-like nature of the resonance whereas an increase in the width of a resonating aperture causes a minor redshift in the resonance wavelength of the aperture as well as it increases the bandwidth and decreases the quality factor of the resonance of the aperture. We have also observed that the resonance behavior of the apertures depends on the light polarization, and a resonance occurs only for the light having an electric field component pointing along the apertures' short axis. In addition, one may observe that apertures placed in a thicker lossy metal film have reduced transmission. Also, significant redshift in the resonance wavelength can be expected by adding a dielectric inside the apertures. Finally, while the fields are concentrated in the interior of the resonant apertures in this structure, the fields can be concentrated at the exit of the apertures by placing the structure on a high-index material.⁵⁷ These observations lead to a series of very straightforward design rules for constructing additional planar spectral light separators based on the approach shown here.

So far, we have shown that our 3D planar subwavelength spectral light separator can achieve spectral decomposition at a subwavelength scale by showing the simulation results of an isolated structure. Given the trend in a detector pixel scaling toward (sub)wavelength size, our device naturally fits within a single pixel. In real-life applications, such as for image sensor or photodetector arrays, our device would most likely be used in an array configuration. Thus, now, we show that an array formed by subwavelength-size unit cells including our structures also achieves a very efficient spectral light separation. The period of the array is not a major design parameter for the operation of our device since the device operation is based on the localized cavity resonances associated with Fabry-Pérot-like modes.^{44,51,52} We also show that the device functionality is angularly robust, that is, the device achieves spectral separation for a very large range of angle of incidence.

Figure 4 illustrates a periodic planar subwavelength spectral light separator. The device is again based on a thin aluminum film with three pairs of apertures. Except for the addition of periodicity, all dimensions are the same as the structure in Figure 1. The period of our periodic structure is 1.75 μm in both the x -direction and the y -direction. This is subwavelength for the operation wavelength range, and the periodicity has only a minor influence on the operation of the device. We again use the FDFD method to examine this periodic structure. This time, in addition to normally incident plane waves, we also use obliquely incident plane waves to excite the structure. Each possible incident plane wave can be decomposed to the basis of s - and p -polarized plane waves in this configuration. Therefore, we perform simulations for both s -polarized incident light (a plane wave with its electric field being perpendicular to plane of incidence) and p -polarized incident light (a plane wave with its magnetic field being perpendicular to plane of incidence). Without a loss of generality, we choose the top and bottom surfaces of our planar structure to be parallel to the xy -plane

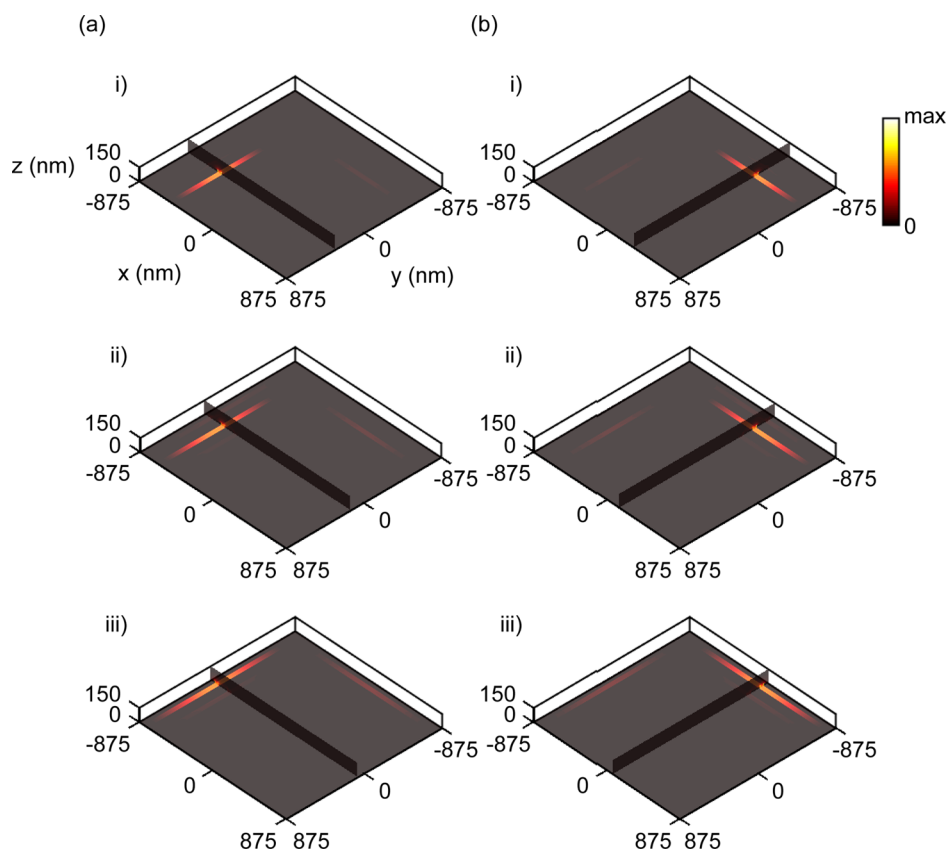


Figure 3. Electric field intensity ($|E|^2$) distributions of the aluminum planar subwavelength spectral light separator excited by a normally incident plane wave for two different polarizations. The incident light is x -polarized in (a), and y -polarized in (b). Subfigures i)–iii) show the intensity distributions when the wavelength of the light is equal 2688 nm, 3328 nm, and 3936 nm, which are the free-space resonance wavelengths of the first, second, and third aperture pair (aperture pairs 1–1', 2–2', and 3–3' in Figure 1), respectively. The origin of the coordinate system corresponds to the center of the structure. The structure is in the region where $-25 \text{ nm} \leq z \leq 25 \text{ nm}$, and it goes towards the $+z$ -direction. In each subfigure, the field intensity is plotted both on the horizontal plane at $z = 0$ which goes through the middle of the structure, and on the vertical plane which goes through the middle of the long side of the resonating aperture. The color scale is chosen such that the maximum of each subfigure corresponds to the same color.

and perpendicular to the z -axis. The plane of incidence is defined by the z -axis and propagation direction. Therefore, the direction of the electric field in s -polarized light (the magnetic field in p -polarized light) is parallel to the xy -plane. In each simulation, we excite the device using an incident plane wave with a different polar angle (θ) and azimuthal angle (φ). The polar angle is defined from the $+z$ -axis direction toward the direction of propagation vector, and hence, it also corresponds to the angle of incidence. The azimuthal angle is defined from the $+y$ -axis direction toward the direction of propagation vector projection on the xy -plane. Since the electric field direction, magnetic field direction and the propagation direction must be orthogonal in a plane wave, the azimuthal angle also corresponds to the angle defined from the $+x$ -axis direction toward the direction of the electric field of the incident light when the incident light is s -polarized. Similarly, it also corresponds to the angle defined from the $+x$ -axis direction toward the direction of the magnetic field of the incident light when the incident light is p -polarized.

While an isolated structure is typically characterized by its transmission cross section,⁵⁵ a periodic structure is characterized by its transmittance as the overall active area of a periodic structure can be clearly defined in each period as the area of the period. Here, we measure the individual transmittances as a function of wavelength.

Figure 5a shows the individual transmittance spectra found for s -polarized incident plane wave with different polar (θ) angle. Here, the azimuthal angle (φ) is fixed and it is 0° . Thus, the direction of the electric field of the incident light is fixed along the x -direction. Hence, s -polarized plane wave here corresponds to x -polarized plane wave. Only the angle of incidence (θ) is changed. The individual transmittance spectra in Figure 5a,i–iii show clear resonance behavior as associated with the first (aperture 1), second (aperture 2), and third (aperture 3) aperture oriented along the y -direction, respectively. This result shows that our device separates the different spectral components of s -polarized light into different apertures for a very large range of angle of incidence. In general, the transmittance values decrease with the increase in the polar angle (angle of incidence). For small angles ($\theta \leq 15^\circ$), however, the decrease is barely noticeable and the transmittance spectra are nearly identical. Also, the resonance wavelengths for different polar angles are very close to each other. These are due to the nearly dipole radiation profile of resonating apertures in our structure, which results in excellent angular robustness of our structure's spectral response and increases the efficiency of our device. We also observe that the longer resonating apertures have higher peak values in their individual transmittance spectra. Another observation made from Figure 5a is that the individual transmittance spectra

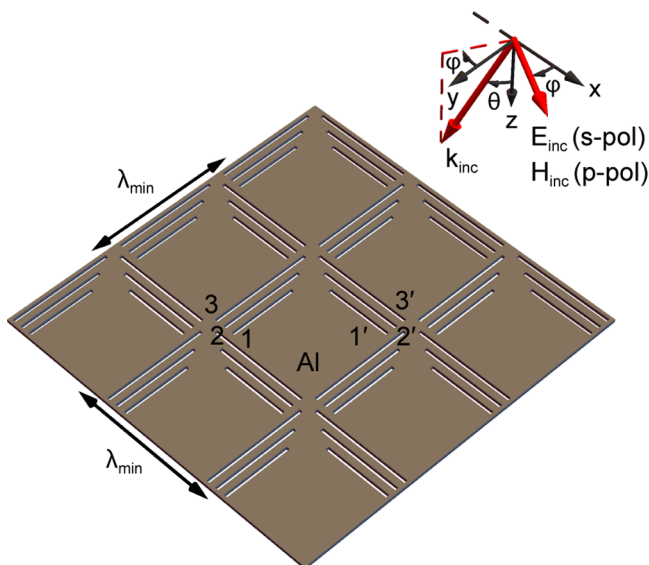


Figure 4. Aluminum planar subwavelength spectral light separator array. It has the same geometry and material as in Figure 1, but this structure is periodic. The periods in the x - and y -directions are the same, both being $1.75 \mu\text{m}$. λ_{min} is $2.3 \mu\text{m}$, which corresponds to the minimum free-space wavelength size in the investigated spectral range. k_{inc} represents the incident light which is an obliquely incident plane wave whose propagation direction is defined by polar (θ) and azimuthal (φ) angle. θ is defined from the $+z$ -direction toward the propagation direction, and it also corresponds to angle of incidence. φ is defined from the $+y$ -direction toward the direction of propagation vector projection on the xy -plane. If the incident light is s -polarized, its electric field is on the xy -plane, whereas if the incident light is p -polarized, its magnetic field is on the xy -plane. Since the electric field direction, magnetic field direction and the propagation direction of a plane wave must be orthogonal, φ also corresponds to the angle defined from the $+x$ -axis direction toward the direction of the electric field of the incident light for s -polarization (the magnetic field of the incident light for p -polarization).

associated with the apertures oriented along the x -direction (apertures 1', 2', and 3') show negligible transmission. This is expected as the wavelength range is above the cutoff wavelengths of these apertures for incident light with electric field along the x -direction.

Figure 5b shows the individual transmittance spectra found for s -polarized incident light with different azimuthal (φ) angles, while the polar angle (θ) is fixed and it is 15° . In this case, the direction of the electric field of the incident light is changed. The individual transmittance spectra in Figure 5b,i–iii show clear resonance behavior as associated with the first, second, and third aperture pair, respectively. At a resonance wavelength, depending on the electric field direction of the incident light, either only one aperture or both apertures of the aperture pair associated with that resonance wavelength can resonate. For example, when $\varphi = 0^\circ$, only apertures oriented along the y -direction resonate. However, when φ increases toward 90° , the resonance at the apertures oriented along the y -direction decreases whereas the resonance at the apertures oriented along the x -direction increases. When $0^\circ \leq \varphi < 45^\circ$ and $135^\circ < \varphi < 225^\circ$ and $315^\circ < \varphi \leq 360^\circ$, the apertures oriented along the y -direction have higher transmittance values than the ones along the x -direction. However, when $45^\circ < \varphi < 135^\circ$ and $225^\circ < \varphi < 315^\circ$, the apertures along the x -direction have higher transmittance values than the ones along the y -

direction. Thus, Figure 5 shows that for a very large range of angle of incidence (θ), our device spectrally separates s -polarized incident light, and it collects different spectral components in different subwavelength-size aperture pairs. Achieving spectral separation is independent of field directions of s -polarized plane waves while using aperture pairs as detected elements. Our device further separates the different linear polarization components of s -polarized incident light and transmits the power of those components through different apertures of aperture pairs.

We repeated the same simulation cases of Figure 5, but this time we used a p -polarized incident plane wave instead. The results are shown in Figure 6. Figure 6a shows the individual transmittance spectra found for a p -polarized incident plane wave with different polar angle (θ). Here, the azimuthal angle is again fixed and it is 0° . Thus, the direction of the magnetic field of the incident light is fixed along the x -direction. Hence, the p -polarized plane wave here has electric field only in the y - and z -directions when $\theta > 0^\circ$ and it corresponds to y -polarized plane wave for $\theta = 0^\circ$. Now, we observe that the individual transmittance spectra in Figure 6a,i–iii show clear resonance behavior as associated with the first (aperture 1'), second (aperture 2'), and third (aperture 3') aperture oriented along the x -direction, respectively. This result shows that our device separates the different spectral components of p -polarized light into different apertures for a very large range of angle of incidence, which confirms the angular robustness of our structure. We notice that the transmittance spectra for the cases with $\theta = 0^\circ$ and $\theta = 15^\circ$ are very close. But, this time, we see a redshift in the resonance wavelength of the small aperture with an increase in the angle of incidence. This is particularly noticeable for $\theta = 30^\circ$ and 45° . We again observe that the longer resonating apertures have higher peak values in their individual transmittance spectra. Another observation made from Figure 6a is that individual transmittance spectra associated with the apertures oriented in the y -direction (apertures 1, 2, and 3) show negligible transmission. This is expected as the wavelength range is above the cutoff wavelengths of these apertures for the incident light with magnetic field along the x -direction.

Figure 6b shows the transmittance spectra found for a p -polarized incident light with different azimuthal (φ) angle, while the polar angle (θ) is fixed and it is 15° . Hence, the direction of the magnetic field component of the incident light is changed. Similarly to the individual transmittance spectra in Figure 5b, the individual transmittance spectra in Figure 6b,i–iii also show clear resonance behavior as associated with the first, second, and third aperture pair, respectively. But this time, the larger resonances for each investigated φ case are associated with the apertures oriented along the x -direction because of the use of p -polarized incident light. But, again, by changing φ , we can increase the resonances in apertures oriented along the y -direction. All other main features are the same as in Figure 5b. Thus, Figure 6 shows that for a very large range of angle of incidence (θ), our device spectrally separates also p -polarized incident light, and it collects the different spectral components in different subwavelength-size aperture pairs. Achieving spectral separation is independent of field directions of p -polarized plane waves when using aperture pairs as detected elements. Our device further separates the different linear polarization components of p -polarized incident light and transmits the power of those components through different apertures of aperture pairs.

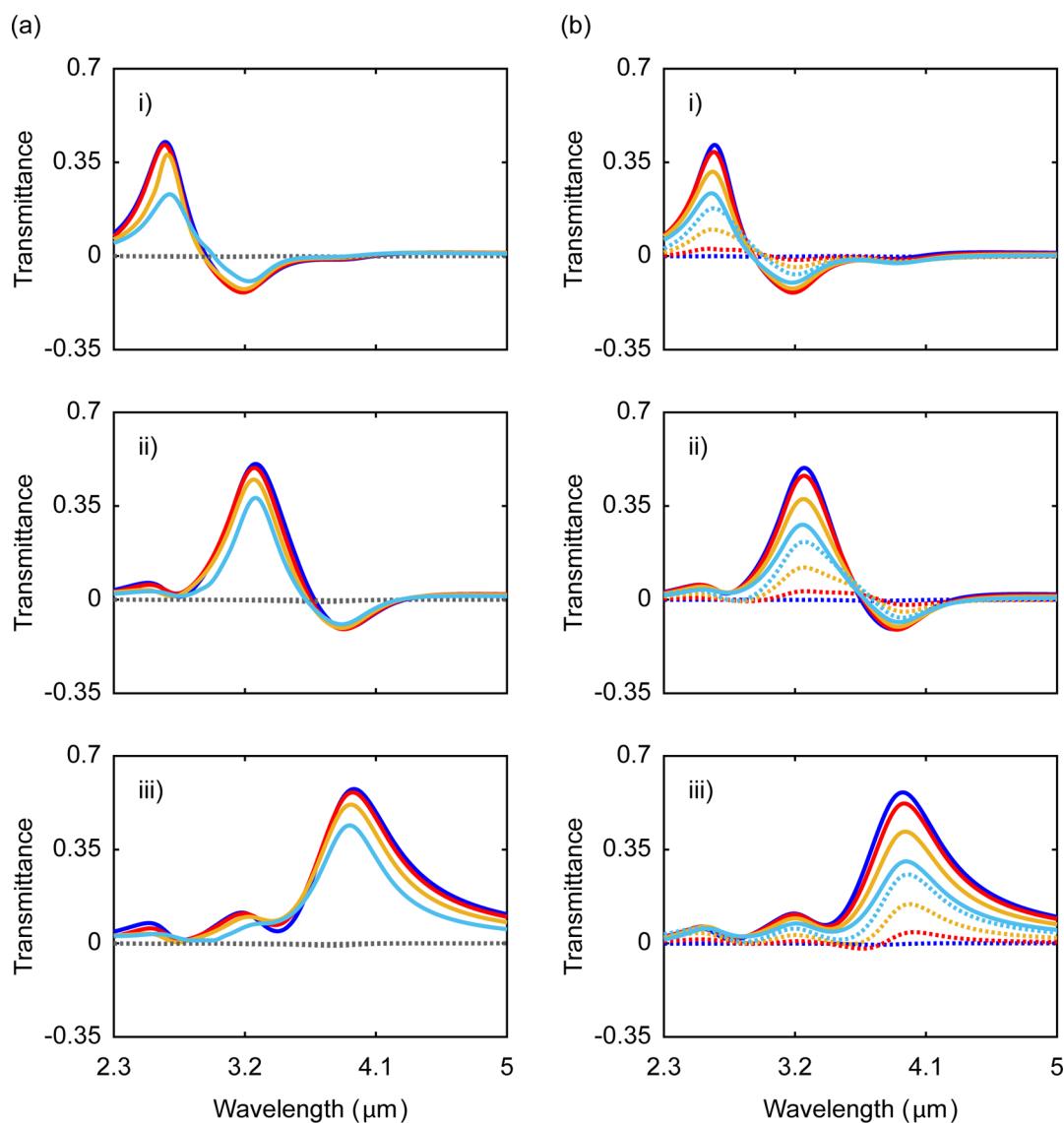


Figure 5. Transmittance spectra of the aluminum planar subwavelength spectral light separator array for *s*-polarized incident light with different polar (θ) and azimuthal (φ) angles. (a) Individual transmittance spectra for the aperture pair 1–1' in (i), 2–2' in (ii), and 3–3' in (iii), while φ is fixed at 0° and θ is changed. The blue, red, orange, and cyan lines show the individual transmittance spectra of the aperture 1 in (i), 2 in (ii), and 3 in (iii) for $\theta = 0^\circ$, $\theta = 15^\circ$, $\theta = 30^\circ$, and $\theta = 45^\circ$, respectively. In each of (i), (ii), and (iii), there are four separate gray dotted lines coinciding almost on top of each other, and they show the individual transmittance spectra of the aperture 1' in (i), 2' in (ii), and 3' in (iii) for $\theta = 0^\circ$, $\theta = 15^\circ$, $\theta = 30^\circ$, and $\theta = 45^\circ$. (b) Individual transmittance spectra for the aperture pair 1–1' in (i), 2–2' in (ii), and 3–3' in (iii), while θ is fixed at 15° and φ is changed. In each of (i), (ii), and (iii), the blue, red, orange, and cyan lines show the individual transmittance spectra for $\varphi = 0^\circ$, $\varphi = 15^\circ$, $\varphi = 30^\circ$, and $\varphi = 42^\circ$, respectively. Solid lines correspond to the aperture 1 in (i), 2 in (ii), and 3 in (iii), and the dotted lines correspond to the aperture 1' in (i), 2' in (ii), and 3' in (iii).

The results obtained from Figures 5 and Figure 6 together show that for a very large range of angle of incidence, achieving the decomposition of incident light into its different spectral components does not depend on the polarization of the light. It also shows that the light components having electric field in the *x*-direction and the light components having electric field in the *y*-direction excite different apertures of aperture pairs, so their power is collected in and transmitted through different apertures.

We also note that when $\theta = 0^\circ$ and $\varphi = 0^\circ$, *s*-polarized light is the same as *x*-polarized light and *p*-polarized light is the same as *y*-polarized light, and our structure is symmetric with respect to a plane that is parallel to the $x = y$ plane. Hence, as complementary to our observations in the isolated structure

response, when $\theta = 0^\circ$ and $\varphi = 0^\circ$, it can be seen from Figure 5a and Figure 6a that the transmittance response of an aperture oriented along the *y*-direction for *s*-polarized illumination and the response of the same-size aperture oriented along the *x*-direction for *p*-polarized illumination are the same.

Once the transmittance spectra of our device are known for both *s*- and *p*-polarized incident light, we can obtain the transmittance spectra of our device for unpolarized light. Figure 7 shows the result for normally incident unpolarized light. The different curves represent the individual transmittance spectra of the different aperture pairs. The peak transmittance values are 0.4253, 0.5072, and 0.5755 for the first (1–1'), second (2–2'), and third (3–3') aperture pair, respectively. This plot shows that our device can decompose unpolarized light into its

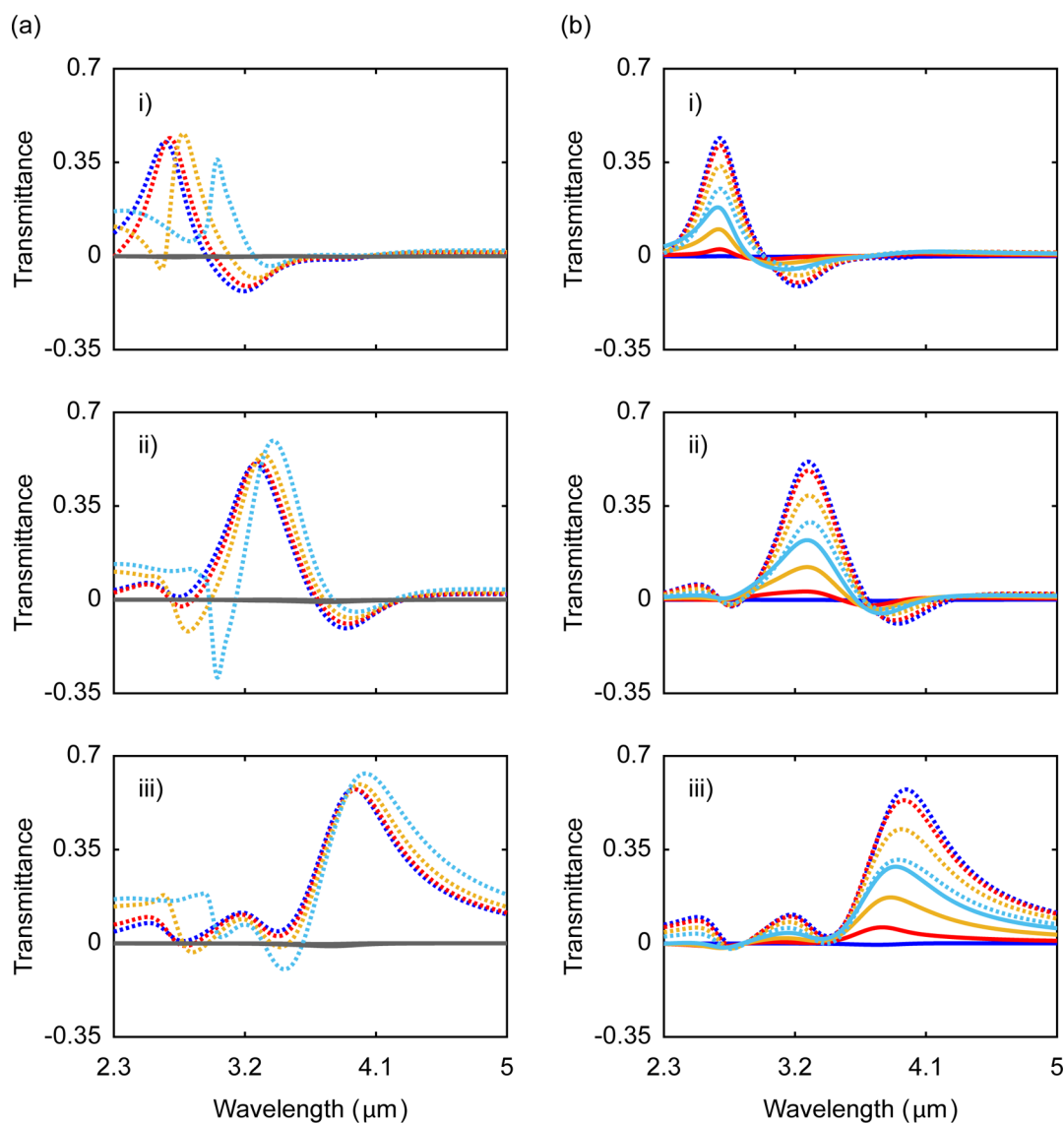


Figure 6. Transmittance spectra of the aluminum planar subwavelength spectral light separator array for *p*-polarized incident light with different polar (θ) and azimuthal (φ) angles. (a) The individual transmittance spectra for the aperture pair 1–1' in (i), 2–2' in (ii), and 3–3' in (iii), while φ is fixed at 0° and θ is changed. The blue, red, orange, and cyan lines show the individual transmittance spectra of the aperture 1' in (i), 2' in (ii), and 3' in (iii) for $\theta = 0^\circ$, $\theta = 15^\circ$, $\theta = 30^\circ$, and $\theta = 45^\circ$, respectively. In each of (i), (ii), and (iii), there are four separate gray solid lines coinciding almost on top of each other, and they show the individual transmittance spectra of the aperture 1 in (i), 2 in (ii), and 3 in (iii) for $\theta = 0^\circ$, $\theta = 15^\circ$, $\theta = 30^\circ$, and $\theta = 45^\circ$. (b) Individual transmittance spectra for the aperture pair 1–1' in (i), 2–2' in (ii), and 3–3' in (iii), while θ is fixed at 15° and φ is changed. In each of (i), (ii), and (iii), the blue, red, orange, and cyan lines show the individual transmittance spectra for $\varphi = 0^\circ$, $\varphi = 15^\circ$, $\varphi = 30^\circ$, and $\varphi = 42^\circ$, respectively. The solid lines correspond to the aperture 1 in (i), 2 in (ii), and 3 in (iii), and the dotted lines correspond to the aperture 1' in (i), 2' in (ii), and 3' in (iii).

spectral bands and each band is transmitted through a different aperture pair, which shows that each aperture pair behaves as a separate spectral channel for transmission. For the imaging applications, these spectral bands can be detected by matching a different detector with each aperture pair. For this purpose, subwavelength-size photodetectors might be used under each aperture pair of our device, and there have been some works showing subwavelength-size photodetectors.⁵⁸

The physical areas of the first (1–1'), second (2–2'), and third (3–3') aperture pairs in a single period are 0.1, 0.125, and $0.15 \mu\text{m}^2$, respectively. This means that the physical areas of the first, second, and third aperture pairs cover about 3.27%, 4.08%, and 4.9% of a single period, respectively. However, at resonance, these aperture pairs transmit 42.53%, 50.72%, and

57.55% of light impinging on a single period. Thus, the apertures funnel and transmit the incident light from an electromagnetic cross-sectional area that is much larger than their physical area.

Moreover, since the electromagnetic cross-sectional areas of the aperture pairs are much larger than the physical areas of the aperture pairs as well as the physical areas that are separating the aperture pairs, there exists a very large overlapping region among the cross-sectional areas from which the aperture pairs get their light, which significantly diminishes the spatial coregistration errors among different spectral channels.

We also note here that the individual transmittance spectra in Figures 5, 6, and 7 show spectral regions of negative power flow through the off-resonant apertures near the resonance wave-

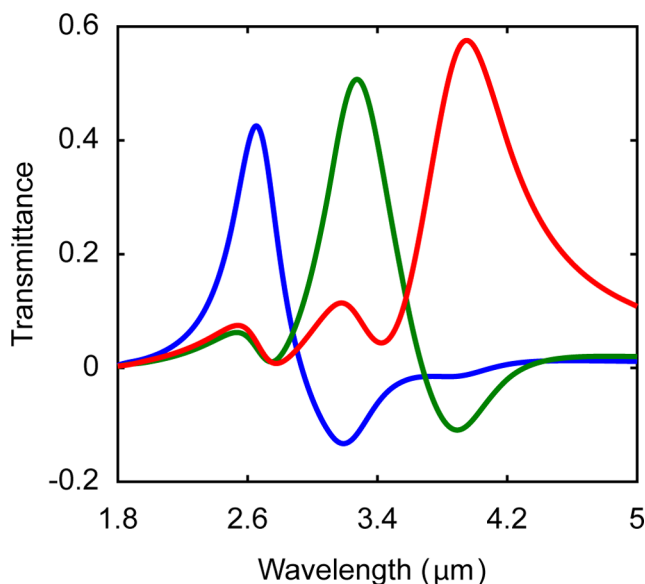


Figure 7. Transmittance spectra of the aluminum planar subwavelength spectral light separator array for normally incident ($\theta = 0^\circ$) unpolarized light. The blue line corresponds to the individual transmittance spectrum of the first aperture pair (1–1'), the green line corresponds to the individual transmittance spectrum of the second aperture pair (2–2'), and the red line corresponds to the individual transmittance spectrum of the third aperture pair (3–3').

lengths, which suggests some minor crosstalk between apertures. Some transmitted power through the resonating apertures flows back to the input side through the off-resonant apertures. We believe that this phenomenon agrees with the previous observations of negative power flow in periodic arrays of compound apertures.⁵⁶ However, we also checked the overall transmittance spectra of an entire period for all the simulated cases in Figures 5, 6, and 7, and observed that all the values of the overall transmittance spectra are above zero. This tells us that even when there is a negative power flow through the off-resonant apertures, the total power flow through the entire structure remains positive, as expected.

One should note that the peak transmittance values in Figure 7 are all above 42% and can almost reach 60%. In comparison, to achieve spectral selectivity, many systems rely on spectral filters, such as spectral filter arrays (SFA),^{4,5,19,59–63} where each pixel records only one spectral component of its input light, which leads to a loss in efficiency. An SFA approach where four separate pixels collect three different spectral components, must have efficiencies less than 25% for at least two spectral components.^{17,20,59} Moreover, in a snapshot system composed of spectral filters, each pixel gets its input light from a separate part of a scene, which necessitates the implementation of spatial interpolation in postprocessing and leads to artifacts and spatial coregistration errors between different spectral channels.^{4,5,11,45,46,62,63} Our device, on the other hand, achieves simultaneous decomposition of incident light into multiple spectral components on the same subwavelength-size pixel area, which drastically reduces spatial coregistration errors and eliminates the need of spatial interpolation. We should also note that our device works better in the spectral ranges where metals have less loss. On the other hand, visible spectrum, where metals have significantly large loss, is also a highly utilized spectral range in imaging applications. That is why we have also tested our device in the visible wavelength range by

scaling the dimensions in our device, and we have not achieved the spectral separation effect due to the higher material loss. However, we guess that by using the concept of assembling several deep-subwavelength resonant structures (“meta-atoms”) formed by different device designs and different materials, such as dielectrics, one might achieve spectral separation in a subwavelength-size device for the visible spectrum. We think that such a device would be a significant alternative to the conventional color filter arrays for imaging applications.

In summary, we have shown a three-dimensional, planar, ultrathin, subwavelength spectral light separator that allows the simultaneous decomposition of incident light into its spectral components. The device operates by utilizing multiple meta-atoms, each supporting a strong, localized resonance. The meta-atoms are based on subwavelength apertures in a metallic film of deep-subwavelength thickness. The device is very photon efficient, which is of great importance in multispectral imaging applications. As a specific example of our device, we have designed an isolated metallic structure with three different rectangular aperture pairs, where each aperture pair is composed of two perpendicularly oriented, same-size apertures; and we have shown that each aperture pair effectively transmits light in a different spectral range. In our device, electromagnetic fields are concentrated in a different aperture pair in each resonance wavelength. Additionally, spatial coregistration errors between different spectral channels are quite reduced since the areas from which the resonant aperture pairs collect their light significantly overlap. We have shown that our device can operate as a single, non-periodic device since it achieves spectral separation of light without relying on any mechanism that depends on periodicity; that being said, we have also demonstrated that our device can operate also in an array configuration composed of subwavelength-size unit cells. Furthermore, we have shown that achieving spectral separation is robust and independent of light polarization for a very large range of angle of incidence while using aperture pairs as detected elements. As a result of all these features, our device suggests a photon-efficient alternative to absorptive spectral filter arrays in multispectral imaging applications. Finally, we have demonstrated that our device also simultaneously separates different linear polarization components of light, and collects their power in different apertures of aperture pairs. This might be useful in applications that require selecting light with a particular linear polarization, or particular electromagnetic field components, in addition to a particular frequency.

METHODS

To simulate the devices shown in Figures 1 and 4, we use the finite-difference frequency-domain (FDFD) method.^{48–50} Unlike time-domain methods, such as the finite-difference time-domain method, the FDFD method allows us to use experimentally measured dielectric constants for dispersive materials such as aluminum⁴⁷ without approximation.

To simulate an infinite space in which the operation of a single isolated (i.e., nonperiodic) device shown in Figure 1 is examined, the finite simulation domain is surrounded in all dimensions (six boundary surfaces) by stretched-coordinate perfectly matched layers (SC-PMLs).^{49,50} To simulate the periodic device shown in Figure 4, SC-PMLs are applied only for the top and bottom boundaries of the simulation domain, and the Bloch boundary conditions are applied at the four remaining sides of the domain.^{64,65} In both cases, the

simulation domain sizes are chosen such that there are enough distances between SC-PMLs and the apertures.

For the single isolated device shown in Figure 1, we calculate the individual transmission cross section spectra of each aperture and the overall transmission cross section spectra of the entire device. To calculate the individual transmission cross section of each aperture, we first locally measure the transmitted power flux through each aperture on a rectangular observation area at the exit of the aperture. The size of each observation area is chosen such that the measured power flux through it corresponds to the transmitted power flux through the corresponding aperture only. Then, the individual transmission cross section of each aperture is obtained by normalizing the transmitted power flux through each aperture with respect to the power flux density of the incident light. To calculate the overall transmission cross section of the entire device, we measure the transmitted power flux through the entire structure, and normalize it with respect to the power flux density of the incident light. Then, to obtain Figure 2, we also perform these calculations for another simulation case where the device material is PEC, and all the other parameters are the same as the device shown in Figure 1.

For the periodic device shown in Figure 4, we calculate the individual transmittance spectra of each aperture. The individual transmittance of an aperture is calculated based on the locally measured power flux transmitted through that aperture only. To calculate the individual transmittance of each aperture, we first locally measure the transmitted power flux through each individual aperture on a rectangular observation area at the exit of each aperture. The size of each observation area is chosen such that the measured power flux through it corresponds to the transmitted power flux through the corresponding aperture only. Then, the individual transmittance of each aperture is obtained by normalizing the transmitted power flux through each aperture with respect to the incident power flux impinging on the entire device in a single period.

AUTHOR INFORMATION

Corresponding Authors

*E-mail: buyukalp@stanford.edu.

*E-mail: pcatryss@stanford.edu.

*E-mail: shanhui@stanford.edu.

ORCID

Yasin Buyukalp: 0000-0003-0354-927X

Peter B. Catrysse: 0000-0002-2389-6044

Present Address

[†]Department of Mathematics, Massachusetts Institute of Technology, Cambridge, Massachusetts 02139, U.S.A.

Notes

The authors declare no competing financial interest.

ACKNOWLEDGMENTS

This work was supported in part by Samsung Electronics.

REFERENCES

- (1) Bao, J.; Bawendi, M. G. A Colloidal Quantum Dot Spectrometer. *Nature* **2015**, *523*, 67–70.
- (2) Redding, B.; Liew, S. F.; Sarma, R.; Cao, H. Compact Spectrometer Based on a Disordered Photonic Chip. *Nat. Photonics* **2013**, *7*, 746–751.

- (3) Yang, T.; Xu, C.; Ho, H.; Zhu, Y.; Hong, X.; Wang, Q.; Chen, Y.; Li, X.; Zhou, X.; Yi, M.; Huang, W. Miniature Spectrometer Based on Diffraction in a Dispersive Hole Array. *Opt. Lett.* **2015**, *40*, 3217–3220.
- (4) Lapray, P.-J.; Wang, X.; Thomas, J.-B.; Gouton, P. Multispectral Filter Arrays: Recent Advances and Practical Implementation. *Sensors* **2014**, *14*, 21626–21659.
- (5) Hagen, N.; Kudenov, M. W. Review of Snapshot Spectral Imaging Technologies. *Opt. Eng.* **2013**, *52*, 90901.
- (6) Tack, N.; Lambrechts, A.; Soussan, P.; Haspeslagh, L. A Compact, High-Speed, and Low-Cost Hyperspectral Imager. *Proc. SPIE* **2012**, *8266*, 82660Q.
- (7) Büyükalp, Y.; Catrysse, P. B.; Shin, W.; Fan, S. Spectral Light Separator Based on Deep-Subwavelength Resonant Apertures in a Metallic Film. *Appl. Phys. Lett.* **2014**, *105*, 11114.
- (8) Catrysse, P. B. Integration of Optical Functionality for Image Sensing through Sub-Wavelength Geometry Design. *Proc. SPIE* **2015**, *9481*, 948102–948108.
- (9) Su, L.; Zhou, Z.; Yuan, Y.; Hu, L.; Zhang, S. A Snapshot Light Field Imaging Spectrometer. *Optik* **2015**, *126*, 877–881.
- (10) Horstmeyer, R.; Athale, R.; Euliss, G. Modified Light Field Architecture for Reconfigurable Multimode Imaging. *Proc. SPIE* **2009**, *7468*, 746804.
- (11) Prieto-Blanco, X.; Montero-Orille, C.; Couce, B.; de la Fuente, R. Optical Configurations for Imaging Spectrometers. In *Computational Intelligence for Remote Sensing; Studies in Computational Intelligence*; Graña, M., Duro, R., Eds.; Springer-Verlag: Berlin; Heidelberg, 2008; pp 1–25.
- (12) Lu, G.; Fei, B. Medical Hyperspectral Imaging: A Review. *J. Biomed. Opt.* **2014**, *19*, 10901.
- (13) Zhang, S.; Ye, Z.; Wang, Y.; Park, Y.; Bartal, G.; Mrejen, M.; Yin, X.; Zhang, X. Anti-Hermitian Plasmon Coupling of an Array of Gold Thin-Film Antennas for Controlling Light at the Nanoscale. *Phys. Rev. Lett.* **2012**, *109*, 193902.
- (14) Piggott, A. Y.; Lu, J.; Lagoudakis, K. G.; Petykiewicz, J.; Babinec, T. M.; Vučković, J. Inverse Design and Demonstration of a Compact and Broadband on-Chip Wavelength Demultiplexer. *Nat. Photonics* **2015**, *9*, 374–377.
- (15) Buyukalp, Y.; Catrysse, P. B.; Shin, W.; Fan, S. Spectral Light Separator: The Subwavelength-Size Device to Spectrally Decompose Light in an Efficient Way. *Proc. Frontiers in Optics 2015*; Optical Society of America, 2015; p FM1B.6.
- (16) Keiser, G. E. A Review of WDM Technology and Applications. *Opt. Fiber Technol.* **1999**, *5*, 3–39.
- (17) Laux, E.; Genet, C.; Skauli, T.; Ebbesen, T. W. Plasmonic Photon Sorters for Spectral and Polarimetric Imaging. *Nat. Photonics* **2008**, *2*, 161–164.
- (18) van Hulst, N. F. Plasmonics: Sorting Colours. *Nat. Photonics* **2008**, *2*, 139–140.
- (19) Xu, T.; Wu, Y.-K.; Luo, X.; Guo, L. J. Plasmonic Nanoresonators for High-Resolution Colour Filtering and Spectral Imaging. *Nat. Commun.* **2010**, *1*, 1–5.
- (20) Sounas, D. L.; Alu, A. Color Separation through Spectrally-Selective Optical Funneling. *ACS Photonics* **2016**, *3*, 620–626.
- (21) Hagen, N.; Kester, R. T.; Gao, L.; Tkaczyk, T. S. Snapshot Advantage: A Review of the Light Collection Improvement for Parallel High-Dimensional Measurement Systems. *Opt. Eng.* **2012**, *51*, 111702.
- (22) Rhodes, H.; Agranov, G.; Hong, C.; Boettiger, U.; Mauritzson, R.; Ladd, J.; Karasev, I.; McKee, J.; Jenkins, E.; Quinlin, W.; Patrick, I.; Li, J.; Fan, X.; Panicci, R.; Smith, S.; Mouli, C.; Bruce, J. CMOS Imager Technology Shrinks and Image Performance. *Proc. 2004 IEEE Workshop on Microelectronics and Electron Devices*; IEEE, 2004; pp 7–18.
- (23) Agranov, G.; Smith, S.; Mauritzson, R.; Chieh, S.; Boettiger, U.; Li, X.; Fan, X.; Dokoutchaev, A.; Gravelle, B.; Qian, H. L. W.; Johnson, R. Pixel Continues to Shrink... Small Pixels for Novel CMOS Image Sensors. *Proc. 2011 International Image Sensor Workshop*; IEEE, 2011.

- (24) Hirayama, T. The Evolution of CMOS Image Sensors. *Proc. 2013 IEEE Asian Solid-State Circuits Conference (A-SSCC)*; IEEE, 2013; pp 5–8.
- (25) Teranishi, N.; Watanabe, H.; Ueda, T.; Sengoku, N. Evolution of Optical Structure in Image Sensors. *Proc. 2012 IEEE International Electron Devices Meeting, IEDM*; IEEE, 2012; pp 533–536.
- (26) Rogalski, A. Recent Progress in Infrared Detector Technologies. *Infrared Phys. Technol.* **2011**, *54*, 136–154.
- (27) Catrysse, P. B.; Skauli, T. Pixel Scaling in Infrared Focal Plane Arrays. *Appl. Opt.* **2013**, *52*, C72–C77.
- (28) Rosenblatt, D.; Sharon, A.; Friesem, A. A. Resonant Grating Waveguide Structures. *IEEE J. Quantum Electron.* **1997**, *33*, 2038–2059.
- (29) Wang, S. S.; Magnusson, R. Theory and Applications of Guided-Mode Resonance Filters. *Appl. Opt.* **1993**, *32*, 2606–2613.
- (30) Chen, Q.; Cumming, D. R. S. High Transmission and Low Color Cross-Talk Plasmonic Color Filters Using Triangular-Lattice Hole Arrays in Aluminum Films. *Opt. Express* **2010**, *18*, 14056–14062.
- (31) Kanamori, Y.; Shimonon, M.; Hane, K. Fabrication of Transmission Color Filters Using Silicon Subwavelength Gratings on Quartz Substrates. *IEEE Photonics Technol. Lett.* **2006**, *18*, 2126–2128.
- (32) Collin, S.; Vincent, G.; Haidar, R.; Bardou, N.; Rommeluère, S.; Pelouard, J.-L. Nearly Perfect Fano Transmission Resonances through Nanoslits Drilled in a Metallic Membrane. *Phys. Rev. Lett.* **2010**, *104*, 27401.
- (33) Barnes, W. L.; Dereux, A.; Ebbesen, T. W. Surface Plasmon Subwavelength Optics. *Nature* **2003**, *424*, 824–830.
- (34) Genet, C.; Ebbesen, T. W. Light in Tiny Holes. *Nature* **2007**, *445*, 39–46.
- (35) Lansey, E.; Hooper, I. R.; Gollub, J. N.; Hibbins, A. P.; Crouse, D. T. Light Localization, Photon Sorting, and Enhanced Absorption in Subwavelength Cavity Arrays. *Opt. Express* **2012**, *20*, 24226–24236.
- (36) Mandel, I. M.; Lansey, E.; Gollub, J. N.; Sarantos, C. H.; Akhmechet, R.; Golovin, A. B.; Crouse, D. T. Photon Sorting in the near Field Using Subwavelength Cavity Arrays in the near-Infrared. *Appl. Phys. Lett.* **2013**, *103*, 251116.
- (37) Lee, H.-S.; Yoon, Y.-T.; Lee, S.; Kim, S.-H.; Lee, K.-D. Color Filter Based on a Subwavelength Patterned Metal Grating. *Opt. Express* **2007**, *15*, 15457–15463.
- (38) Pelzman, C.; Cho, S.-Y. Plasmonic Metasurface for Simultaneous Detection of Polarization and Spectrum. *Opt. Lett.* **2016**, *41*, 1213–1216.
- (39) Yokogawa, S.; Burgos, S. P.; Atwater, H. A. Plasmonic Color Filters for CMOS Image Sensor Applications. *Nano Lett.* **2012**, *12*, 4349–4354.
- (40) Haïdar, R.; Vincent, G.; Collin, S.; Bardou, N.; Guérineau, N.; Deschamps, J.; Pelouard, J.-L. Free-Standing Subwavelength Metallic Gratings for Snapshot Multispectral Imaging. *Appl. Phys. Lett.* **2010**, *96*, 221104.
- (41) Veronis, G.; Min, C.; Huang, Y.; Yang, L. Nanophotonic Resonators for Enhancement of Absorption and Transmission Cross Sections of Subwavelength Plasmonic Devices. In *Integrated Nanophotonic Resonators: Fundamentals, Devices, and Applications*; Yi, Y. S., Ed.; Pan Stanford Publishing, 2015; pp 93–126.
- (42) Le Perche, J.; Desieres, Y.; Rochat, N.; Espiau de Lamaestre, R. Subwavelength Optical Absorber with an Integrated Photon Sorter. *Appl. Phys. Lett.* **2012**, *100*, 113305.
- (43) Park, H.; Dan, Y.; Seo, K.; Yu, Y. J.; Duane, P. K.; Wober, M.; Crozier, K. B. Filter-Free Image Sensor Pixels Comprising Silicon Nanowires with Selective Color Absorption. *Nano Lett.* **2014**, *14*, 1804–1809.
- (44) Ruan, Z.; Qiu, M. Enhanced Transmission through Periodic Arrays of Subwavelength Holes: The Role of Localized Waveguide Resonances. *Phys. Rev. Lett.* **2006**, *96*, 233901.
- (45) Skauli, T. Quantifying Coregistration Errors in Spectral Imaging. *Proc. SPIE* **2011**, 81580A.
- (46) Skauli, T. An Upper-Bound Metric for Characterizing Spectral and Spatial Coregistration Errors in Spectral Imaging. *Opt. Express* **2012**, *20*, 918–933.
- (47) *CRC Handbook of Chemistry and Physics*, 96th ed.; Haynes, W. M., Ed.; CRC Press: Boca Raton, FL, 2015.
- (48) Champagne, N. J.; Berryman, J. G.; Buettnner, H. M. FDFD: A 3D Finite-Difference Frequency-Domain Code for Electromagnetic Induction Tomography. *J. Comput. Phys.* **2001**, *170*, 830–848.
- (49) Shin, W.; Fan, S. Choice of the Perfectly Matched Layer Boundary Condition for Frequency-Domain Maxwell's Equations Solvers. *J. Comput. Phys.* **2012**, *231*, 3406–3431.
- (50) Shin, W.; Fan, S. Accelerated Solution of the Frequency-Domain Maxwell's Equations by Engineering the Eigenvalue Distribution of the Operator. *Opt. Express* **2013**, *21*, 22578–22595.
- (51) García-Vidal, F. J.; Moreno, E.; Porto, J. A.; Martín-Moreno, L. Transmission of Light through a Single Rectangular Hole. *Phys. Rev. Lett.* **2005**, *95*, 103901.
- (52) García-Vidal, F. J.; Martín-Moreno, L.; Moreno, E.; Kumar, L. K. S.; Gordon, R. Transmission of Light through a Single Rectangular Hole in a Real Metal. *Phys. Rev. B: Condens. Matter Mater. Phys.* **2006**, *74*, 153411.
- (53) García-Vidal, F. J.; Martín-Moreno, L.; Ebbesen, T. W.; Kuipers, L. Light Passing through Subwavelength Apertures. *Rev. Mod. Phys.* **2010**, *82*, 729–787.
- (54) Gordon, R.; Brolo, A. G. Increased Cut-off Wavelength for a Subwavelength Hole in a Real Metal. *Opt. Express* **2005**, *13*, 1933–1938.
- (55) Verslegers, L.; Yu, Z.; Catrysse, P. B.; Fan, S. Temporal Coupled-Mode Theory for Resonant Apertures. *J. Opt. Soc. Am. B* **2010**, *27*, 1947–1956.
- (56) Enemu, A.; Nolan, M.; Uk Jung, Y.; Golovin, A. B.; Crouse, D. T. Extraordinary Light Circulation and Concentration of S- and P-Polarized Phase Resonances. *J. Appl. Phys.* **2013**, *113*, 14907.
- (57) White, J. S.; Veronis, G.; Yu, Z.; Barnard, E. S.; Chandran, A.; Fan, S.; Brongersma, M. L. Extraordinary Optical Absorption through Subwavelength Slits. *Opt. Lett.* **2009**, *34*, 686–688.
- (58) Tang, L.; Kocabas, S. E.; Latif, S.; Okyay, A. K.; Ly-Gagnon, D.-S.; Saraswat, K. C.; Miller, D. A. B. Nanometre-Scale Germanium Photodetector Enhanced by a near-Infrared Dipole Antenna. *Nat. Photonics* **2008**, *2*, 226–229.
- (59) Bayer, B. E. Color Imaging Array. U.S. Patent 3,971,065, 1976.
- (60) Chen, C.-W.; Fuh, C.-S. Lens Shading Correction for Dirt Detection. In *Pattern Recognition, Machine Intelligence and Biometrics*; Wang, P. S. P., Ed.; Springer-Verlag: Berlin; Heidelberg, 2011; pp 171–195.
- (61) Snyder, W. E. A Generic Method for Generating Multispectral Filter Arrays. *2004 International Conference on Image Processing, ICIP 2004*; IEEE, 2004; Vol. 5, pp 3343–3346.
- (62) Gunturk, B. K.; Glotzbach, J.; Altunbasak, Y.; Schafer, R. W.; Mersereau, R. M. Demosaicking: Color Filter Array Interpolation. *IEEE Signal Process. Mag.* **2005**, *22*, 44–54.
- (63) Chang, L. Hybrid Color Filter Array Demosaicking for Effective Artifact Suppression. *J. Electron. Imaging* **2006**, *15*, 13003.
- (64) Fan, S.; Joannopoulos, J. D. Analysis of Guided Resonances in Photonic Crystal Slabs. *Phys. Rev. B: Condens. Matter Mater. Phys.* **2002**, *65*, 235112.
- (65) Taflove, A.; Hagness, S. C. *Computational Electrodynamics: The Finite-Difference Time-Domain Method*, 3rd ed.; Artech House: Norwood, MA, 2005.